Dual-Band Transmissive Metasurface With Independent Amplitude and Phase Control for Low Sidelobe Antenna Application

Weikang Li, Xinwei Chen, Wubin Niu, Liping Han, and Wenmei Zhang, *Senior Member, IEEE*

***Abstract*—In this letter, a dual-band transmissive metasurface (MS) with independent amplitude and phase control is proposed. The element is formed by three metal layers separated by two substrates. The top and bottom layers are orthogonal metal gratings, and the middle layer is a patch etched with two double-split ring resonators (DSRRs) and an annular slot. By tuning the geometries and orientations of the outer and inner DSRR, the amplitude and phase in lower and higher bands can be regulated, respectively. The annular slot improves the amplitude of the two bands and eliminates the interference between them. Then, two dual-band transmitarrays with phase-only and amplitude/phase modulation MS are fabricated and measured. The former has aperture efficiencies (AEs) of 48.4%/45.8% at (9.2, 17) GHz with 3 dB gain bandwidth of 13% [(8.4 to 9.6) GHz]/7.2% [(16.2 to 17.4) GHz]. The latter achieves AEs of 29.8%/27.0% at (9.1, 17) GHz with 3 dB gain bandwidth of 17.4% [(8.4 to 10) GHz]/7.2% [(16.2 to 17.4) GHz], as its sidelobe levels are suppressed to −24.8 (−22.5 dB)/−26.2 (−24.9 dB) in *xoz*- (*yoz*-) plane.**

***Index Terms*—Dual-band, low sidelobe, metasurface, phase and amplitude modulation, transmitarray antenna (TA).**

I. Introduction

TRANSMITARRAY antenna (TA) is a new type of high-gain antenna, which has attracted growing attention in recent years due to its advantages of lightweight, low cost, high gain and no feed blockage [1], [2], [3], [4], [5]. Moreover, some single-band TAs based on the amplitude and phase adjustable metasurface (MS) have been proposed [6], [7], [8]. In [6], a TA working at 10 GHz is designed. The sidelobe level (SLL) is suppressed below −29 dB by imposing the Taylor amplitude distribution on the aperture. In [8], a wideband TA is designed to generate fan-shaped beams within 9.1 GHz to 10.9 GHz.

To meet the requirement of the integrated system, some dual-band TAs based on the phase modulation MS have been proposed [9], [10], [11], [12], [13], [14], [15]. An example operating at 12/18 GHz is explained in [9] and achieves aperture efficiencies (AEs) of 52%/53% and SLLs of (−13, −16) dB. Another case operating at (11, 12.5) GHz is presented in [10]. Transmission phase of its element can cover $5\pi/6$ with transmission loss of 3 dB in both bands. Also, a generalized method to design dual-band TA is presented in [12]. It uses a seven-layer metal element and exhibits AEs of 32%/28% at (20, 30) GHz. In addition, some orthogonally polarized TAs are presented in [13], [14], and [15], which can be used in the cases where different polarization directions are required in two bands. However, due to lacking amplitude regulation, the aforementioned dual-band TAs can't work in occasions that the power of beam needs to be controlled, such as suppressing SLLs and multibeam forming with arbitrary power allocations. That is, how to realize a dual-band TA with independent amplitude and phase control is still a challenge.

Received 15 July 2024; revised 10 September 2024; accepted 18 September 2024. Date of publication 20 September 2024; date of current version 13 December 2024. This work was supported in part by the National Natural Science Foundation of China under Grant 62071282 and in part by the National Science Foundation of Shanxi Province under Grant 202203021211295, and Grant 202303021221072. *(Corresponding author: Wenmei Zhang.)*

The authors are with the Shanxi Key Laboratory of Wireless Communication and Detection and the School of Physics and Electronic Engineering, Shanxi University, Shanxi 030006, China (e-mail: zhangwm@sxu.edu.cn).

Digital Object Identifier 10.1109/LAWP.2024.3465630

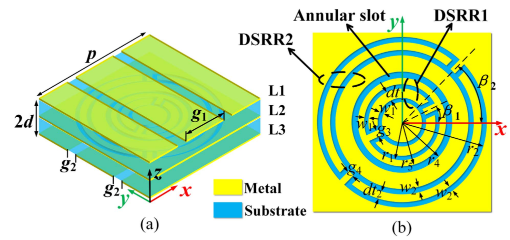

Fig. 1. Geometry of the MS element. (a) 3-D view. (b) Top view of L2 metal layer. (Dimensions: $p = 8.5$, $g_1 = 2.85$, $g_2 = 0.65$, $g_3 = 0.3$, $g_4 = 0.3$, $r_1 = 1.8$, $r_2 = 4.05$, $r_4 = 2.4$, $r_5 = 2.1$, $w_1 = 0.2$, $w_2 = 0.25$, $dt_1 = 0.5$, $dt_2 = 0.4$. Unit: mm).

In this letter, a dual-band (9.3, 17 GHz) transmissive MS with independent amplitude and phase regulation is proposed. The DSRRs for two bands are arranged in a metal sheet to achieve a low profile MS. By introducing an annular slot among two DSRRs, the coupling between them is suppressed. As a result, amplitude and phase in the two bands are controlled independently. Also, the annular slot helps to improve the transmission coefficient, especially that in higher bands. On this basis, two TAs with phase-only and amplitude/phase modulations MS are fabricated and tested. In two bands, the former achieves high AEs of 48.4%/45.8%, and the latter has AEs of 29.8%/27% under the condition of SLLs of (−25, −28) dB.

II. Element Design and Analysis

A. Metasurface Element Design

Fig. 1 illustrates the structure of the dual-band transmissive MS element, which consists of three metal layers (L1, L2, and L3) separated by two F4B substrates ($d = 1$ mm, $\varepsilon_r = 2.2$, $\tan\delta = 0.002$). Layers L1 and L3 are two orthogonal metallic gratings that construct a Fabry–Perot-like cavity to improve

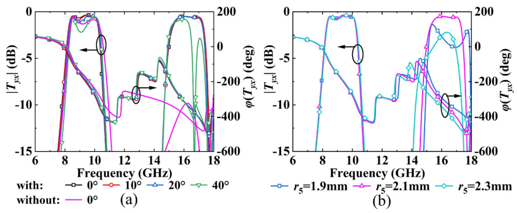

Fig. 2. (a) Simulated amplitude and phase of T_{yx} for element (a) with and without annular slot and (b) with different r_5.

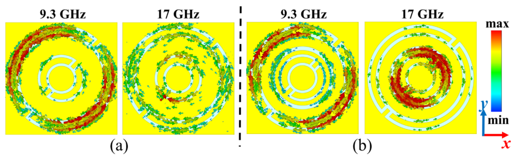

Fig. 3. Simulated surface current distributions of layer L2 of the two elements. (a) Without annular slot. (b) With annular slot.

the polarization conversion efficiency [17], [18], [19]. Layer L1 allows the x-polarized wave from $+z$ direction to pass through and reflects the y-polarized wave, while layer L3 has the opposite effect. Layer L2 shown in Fig. 1(b) is a square patch etched with two double-split ring resonators (DSRR1 and DSRR2) and an annular slot. DSRR2 and DSRR1 are used as polarization conversion structures and their effective perimeter $l_{\mathrm{DSRR2}}/l_{\mathrm{DSRR1}}$ are determined by the center frequency (with the guided-wavelength $\lambda_{\mathrm{L}}/\lambda_{\mathrm{H}}$) of lower/higher band. That is, $l_{\mathrm{DSRR2}} \approx 2\ \lambda_{\mathrm{L}}$ and $l_{\mathrm{DSRR1}} \approx 2\ \lambda_{\mathrm{H}}$. In this case, the wave in other bands can be filtered out with the help of Fabry–Perot-like cavity formed by layers L1 and L3. The annular slot is used to improve the transmission coefficient of the two bands and eliminate the coupling between them. The detailed parameters are listed in the caption of Fig. 1.

The designed element is simulated in CST Microwave Studio. Periodic boundaries are set along both x- and y-directions and Floquet ports are applied along the z-direction. First, the effect of annular slot is investigated and the results are shown in Fig. 2. In Fig. 2(a), when the incident angle is 0°, the cross-polarized transmission amplitude $|T_{yx}|$ of the unit without annular slot remains above -1.41 dB in 8.5 GHz to 10 GHz, but is only -9.6 dB in 16 GHz to 17.5 GHz. After an annular slot is etched, the $|T_{yx}|$ increases to better than -0.73 dB within (8.5, 10) GHz and (16, 17.5) GHz. This indicates that the annular slot plays an important role in improving the transmission amplitude in both bands. Also, with the incident angle increasing to 40°, the amplitude $|T_{yx}|$ slightly decreased and the phase $\varphi(T_{yx})$ changed little. Moreover, the influence of r_4 and r_5 is surveyed. Only the result for r_5 is given in Fig. 2(b) considering that T_{yx} hardly changes with r_4. It is seen that r_5 significantly affects the T_{yx} in the higher band. Finally, $r_5 = 2.1$ mm is selected to obtain the larger $|T_{yx}|$.

Furthermore, the surface current distributions of the above two units are depicted in Fig. 3. From Fig. 3(a), the current is mainly concentrated in the DSRR2 at 9.3 GHz, while weak current appears on the DSRR1 at 17 GHz. After etching an annular slot, as shown in Fig. 3(b), the strong current mainly distributes on DSRR2 and DSRR1 at 9.3 GHz and 17 GHz, respectively. Meanwhile, it can be seen that the surface current crosstalk between two DSRRs is negligible, which indicating the independent control of the two frequency bands.

TABLE I
SPECIFIC DIMENSIONS OF THE 3-BIT ELEMENTS

Code	000	001	010	011	100	101	110	111
w_2(mm)	0.495	0.2	0.275	0.375	0.495	0.2	0.275	0.375
β_2(°)	45	-45	-45	-45	-45	45	45	45

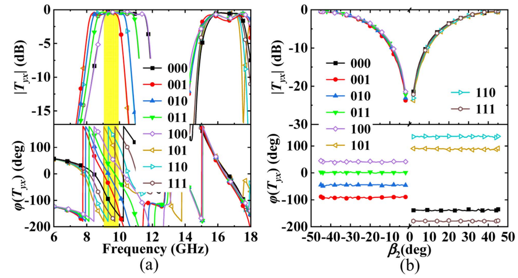

Fig. 4. Simulated amplitude and phase curves of 3-bit elements versus (a) frequency and (b) β_2 at 9.3 GHz.

TABLE II
SPECIFIC DIMENSIONS OF THE 2-BIT ELEMENTS

Code	00	01	10	11
w_1/ dt_1/ g_3 (mm)	0.5/0.2/1.2	0.2/0.95/0.1	0.5/0.2/1.2	0.2/0.95/0.1
β_1 (°)	-45	45	45	-45

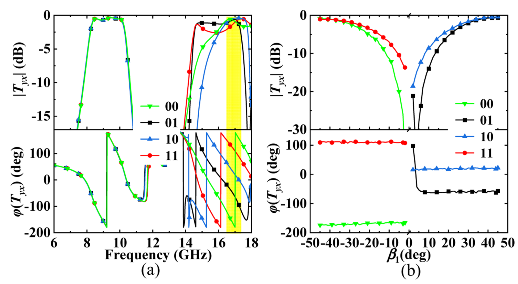

Fig. 5. Simulated amplitude and phase curves of 2-bit elements versus (a) frequency and (b) β_1 at 17 GHz.

B. Dual-band Independent Modulation of Amplitude/Phase

Next, we describe how to independently control the $|T_{yx}|$ and $\varphi(T_{yx})$ in both bands. In the lower band, 3-bit phase and continuous amplitude modulation are achieved by changing the gap width w_2 and rotation angle β_2 of DSRR2, respectively. Table I lists the specific dimensions and the characteristic curves are plotted in Fig. 4. From Fig. 4(a), it can be seen that the $|T_{yx}|$ of eight units are higher than -0.44 dB in the range of 9.1 GHz to 9.8 GHz, and the phase difference between neighboring elements is $\pi/4$. In Fig. 4(b), at 9.3 GHz, the $|T_{yx}|$ of elements change from -23 dB to -0.44 dB with β_2, while the $\varphi(T_{yx})$ remain unchanged. In addition, in the process of phase control, the amplitude curve will move. That is, with the increase of bit number, the operating bandwidth (highlighted in yellow) will be reduced. Considering synthetically quantization errors and bandwidth, the 3-bit phase is chosen. Similar conclusions can be drawn in higher band. In the same way, 2-bit phase and continuous amplitude modulation in the higher band can also be obtained by adjusting the DSRR1. The specific parameters and characteristic curves are given in Table II and Fig. 5, respectively. In the range of 16.7 GHz to 17.2 GHz, the $|T_{yx}|$ of four elements are maintained above -1.9 dB (the $|T_{yx}|$ at 17 GHz are better than -0.91 dB), and the adjacent phase difference is $\pi/2$. Besides,

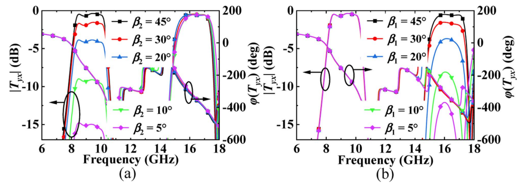

Fig. 6. Simulated amplitude and phase curves of T_{yx} versus frequency with different (a) β_2 and (b) β_1.

TABLE III
COMPARISONS WITH OTHER TRANSMISSIVE MS ELEMENTS

Ref.	Working bands	Band ratio	Freq. (GHz)	Max. Amp. (dB)	Independent Amp. control	Phase range
[16]	Single	\	800	−6.1	Yes	2π
[7]	Single	\	12.2	−1.41-0	Yes	2π
[8]	Single	\	10	−0.91-0	Yes	2π
[9]	Dual	1.50	12	−1.9-0	NO	2π
			18	−1.9-0		2π
[11]	Dual	1.14	12.5	−2.1	NO	$5/6\pi$
			14.25	−2.1		$5/6\pi$
This work	**Dual**	**1.82**	**9.3**	**−0.44**	**Yes**	**3-bit**
			17	**−0.91**	**Yes**	**2-bit**

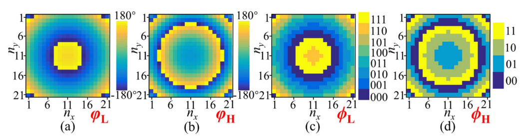

Fig. 7. Simulated compensated phases of (a) φ_{L} and (b) φ_{H}. (c) 3-bit quantized phase ϕ_{L} and (d) 2-bit quantized phase ϕ_{H}.

larger amplitude fluctuations in the higher band are observed during the phase modulation because multiple parameters are adjusted simultaneously and the variation relative to DSRR1 is large. In Fig. 5(b), at 17 GHz, the $|T_{yx}|$ of elements increases with β_1, while the $\varphi(T_{yx})$ remain stable.

Additionally, the crosstalk between the two bands is also investigated. From Figs. 4(a) and 6(a), the $|T_{yx}|$ and $\varphi(T_{yx})$ in the higher band remain stable when w_2 and β_2 of DSRR2 are adjusted. Meanwhile, in Figs. 5(a) and 6(b), the $|T_{yx}|$ and $\varphi(T_{yx})$ in the lower band also keep unchanged when DSRR1 changed.

Table III shows the comparisons between the proposed MS element and other reported transmissive elements. Clearly, the proposed element features the advantages of independent amplitude and phase modulation in both frequency bands and a higher transmission coefficient [(−0.44, −0.91) dB].

III. Dual-Band TAs Design and Measurement

To show the performance of the proposed element, we design TAs with phase-only and phase/amplitude modulations MS and referred as TA_1 and TA_2, respectively. Two standard horns (HD-100SGAH10N, 8.2 GHz to 12.4 GHz; LB-62–10-C-SF, 12.4 GHz to 18 GHz) are adopted as the feeds. To achieve optimal efficiency, we set the aperture size of the MSs as $D = 178.5$ mm (21×21 elements) and the focal distance as $F = 142$ mm.

A. TA_1 With Phase-Only Modulation

In this section, we design an antenna TA_1 with phase-only modulation. First, simulate the feeds and obtain the phases of the electrical field when it arrives in the MS. Then, the compensated phases $\varphi_{\mathrm{L}}/\varphi_{\mathrm{H}}$ at (9.3, 17) GHz, as shown in Fig. 7(a) and (b), are achieved by negating the simulated phases [20], [21], [22].

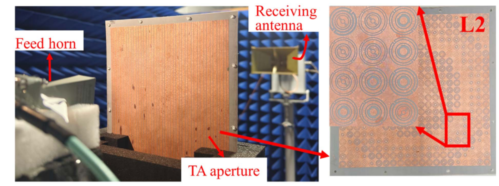

Fig. 8. Photographs of the antenna TA_1 and measurement setup.

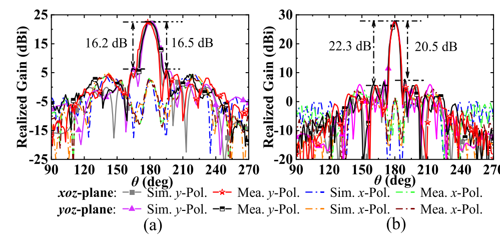

Fig. 9. Simulated and measured radiation patterns of TA_1. (a) 9.3 GHz. (b) 17 GHz.

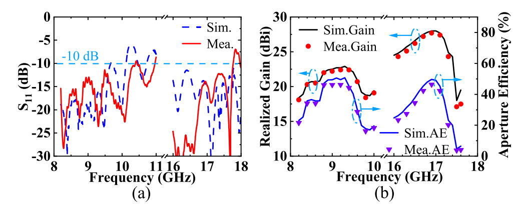

Fig. 10. Simulated and measured bandwidth performance of TA_1. (a) S_{11}. (b) Realized gain and aperture efficiency.

Further, according to Figs. 4 and 5, φ_{L} and φ_{H} are quantified into 3-bit and 2-bit phases at the quantization intervals of $\pi/4$ and $\pi/2$, respectively, and shown in Fig. 7(c) and (d). Finally, the MS sample is fabricated and measured in a microwave anechoic chamber, as displayed in Fig. 8.

Fig. 9 shows the 2-D radiation patterns of TA_1 at 9.3 GHz and 17 GHz. Considering the fabrication tolerances, the simulated and measured results are consistent with each other. The simulated/measured gains at 9.3 GHz and 17 GHz are (22.9, 22.7) dBi and (28, 27.7) dBi, respectively. Also, the corresponding SLLs in the *xoz*- (*yoz*-) plane are (−16.9, −16.5) dB [(−16.5, −16.2) dB] and (−22.8, −21) dB [(−22.3, −20.5) dB], respectively.

Fig. 10 exhibits the bandwidth performance of the TA_1. From Fig. 10(a), the measured S_{11} is lower than −10 dB in the range of (8.2, 10.3) GHz and (16, 17.7) GHz. In Fig. 10(b), the measured 3 dB gain bandwidth is about 13% [(8.4 to 9.6) GHz] and 7.2% [(16.2 to 17.4) GHz]. Also, the peak gains are 22.7 dBi and 27.7 dBi, with AEs of 48.4% and 45.8% at 9.2 GHz and 17 GHz, respectively.

B. TA_2 With Phase and Amplitude Modulations

In the previous section, the TA_1 with phase-only modulation has high SLLs in both bands. Next, based on it, Taylor amplitude modulation is added to reduce the SLLs in two frequency bands. The corresponding antenna is termed as TA_2.

The design process of the antenna TA_2 is shown in Fig. 11. Considering that the initial SLLs of the TA_1 are not equal in two bands, so the designed goals are set as (−25, −28) dB along *x*- and *y*-directions at (9.3, 17) GHz. According to the theory of

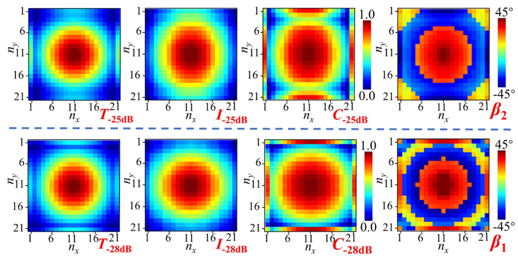

Fig. 11. Design process of TA_2.

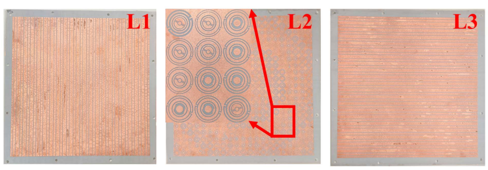

Fig. 12. Photograph of the antenna TA_2.

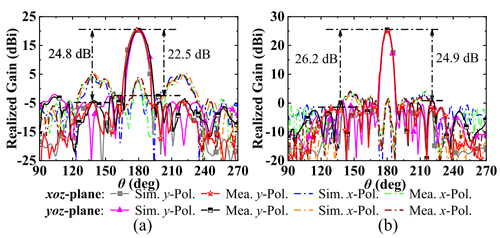

Fig. 13. Simulated and measured radiation patterns of TA_2. (a) 9.3 GHz. (b) 17 GHz.

array antenna, the Taylor distribution is represented as [23]

$$T = T_1 \cdot T_1' \tag{1}$$

$$T_1(m) = 1 + 2 \sum_{i=1}^{m_0 - 1} F_a(i) \cos\left(\frac{2im\pi}{M-1}\right) \tag{2}$$

$$m = \begin{cases} 0, \pm 1, \pm 2, \cdots, \pm \frac{M-1}{2} & M \text{ is odder number} \\ \pm 1, \pm 2, \cdots, \pm \frac{M}{2} & M \text{ is even number} \end{cases} \tag{3}$$

where T and T_1 represent the 2-D and 1-D Taylor distributions on the aperture, respectively, and T_1' is the transpose of T_1. m is the sequence number of the element along the x-axis, and M is the total number of elements on the array. By using (1)–(3), the 2-D Taylor distributions $T_{-25\text{ dB}}$ and $T_{-28\text{ dB}}$ are calculated. Next, the required amplitude of the (xth, yth) element $C_{-25\text{ dB}}(x, y)$ and $C_{-28\text{ dB}}(x, y)$ can be obtained by [23]

$$C_{-25\text{dB}}(x, y) = T_{-25\text{dB}}(x, y) / I_{-25\text{dB}}(x, y) \tag{4}$$

$$C_{-28\text{dB}}(x, y) = T_{-28\text{dB}}(x, y) / I_{-28\text{dB}}(x, y) \tag{5}$$

where $I_{-25\text{ dB}}(x, y)$ and $I_{-28\text{ dB}}(x, y)$ is the normalized amplitude of the two horn antennas on the aperture, respectively. Afterward, the distribution of $C_{-25\text{ dB}}$ and $C_{-28\text{ dB}}$ are transformed into the rotation angles β_2 and β_1, respectively. Once the above two rotation angle distributions are determined, the new antenna TA_2 can be constructed based on the TA_1, as shown in Fig. 12.

The 2-D radiation patterns of TA_2 are shown in Fig. 13. The simulated/measured gains at 9.3 GHz and 17 GHz are (20.9, 20.7) dBi and (25.7, 25.4) dBi, respectively. The corresponding SLLs in the *xoz*- (*yoz*-) plane are (−25.1, −24.8) dB [(−22.7, −22.5) dB] and (−26.6, −26).2 dB [(−25, −)24.9 dB], respectively. Compared with the antenna TA_1, the SLLs in *xoz*-/*yoz*-plane is decreased by (8.3, 6.3) dB and (3.9, 4.4) dB at 9.3 GHz and 17 GHz, respectively, at a price of drop in gain of 2 dBi and 2.3 dBi. This indicates that the proposed dual-band MS with independent amplitude/phase control can suppress the SLLs in both bands simultaneously. In addition, it can be seen that the realized SLLs have a certain discrepancy with the designed goal. These differences are attributed to the amplitude approximation in theoretical design and the mutual coupling between elements.

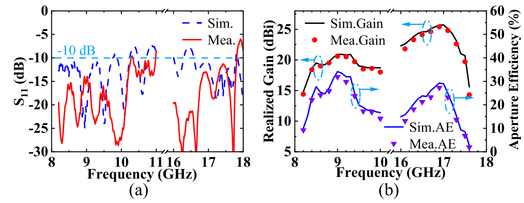

Fig. 14. Simulated and measured bandwidth performance of TA_2. (a) S_{11}. (b) Realized gain and aperture efficiency.

TABLE IV
COMPARISONS WITH OTHER SIMILAR TAS

Ref.	Freq. (GHz)	Panel Thick.	AE (%) POM (PAM)	SLLs (dB) (*xoz-/yoz-*) POM (PAM)	BW (%) POM (PAM)
[7]	12.2	0.08λ	34 (26)	-23.5/-17.5 (-25.3/-23.6)	17.4 (16.4)
[24]	10.3	0.05λ	36 (25)	-12.4/- (-25.9/-)	>8.0(8.0)
[9]	12	0.6λ	52 (\)	-13/- (\)	3.3 (\)
	18	0.9λ	53 (\)	-16.5/- (\)	3.3 (\)
[10]	11	0.47λ	37.2 (\)	-15/-15 (\)	>6.8 (\)
	12.5	0.53λ	34 (\)	-14/-14 (\)	>5.4 (\)
[15]	20	0.1λ	20.1 (\)	-17/-20 (\)	11.3 (\)
	30	0.15λ	21.2 (\)	-19/-19 (\)	11.4 (\)
This work	**9.3**	**0.06λ**	**48.4 (29.8)**	**-16.5/-16.3 (-24.8/-22.5)**	**13 (17.4)**
	17	**0.13λ**	**45.8 (27.0)**	**-22.3/-20.5 (-26.2/-24.9)**	**7.2 (7.2)**

Note: BW: 3 dB gain bandwidth; POM: Phase-Only Modulation; PAM: Phase and Amplitude Modulation;

Fig. 14 plots the bandwidth performance of antenna TA_2. The measured −10 dB bandwidth is in the range of 8.2 GHz to 10.2 GHz and 16 GHz to 17.7 GHz and the 3 dB gain bandwidth is about 17.4% [(8.4 to 10) GHz] and 7.2% [(16.2 to 17.4) GHz]. Also, the peak gains are 20.7 dBi and 25.4 dBi with AEs of 29.8% and 27.0% at 9.1 GHz and 17 GHz, respectively. In addition, it is noted that the measured S_{11} and gains are lower than the simulated results. The former may be caused by frequency shifting downward and the larger loss of the fabricated MS. The latter is due to the fact that part of the energy is converted to the side lobe, resulting in a decrease in the gain of the main lobe.

The comparisons of the proposed TAs and other previous works are listed in Table IV. It is seen that the reported TAs with SLL manipulation in [7] and [24] only operate in single frequency band. The proposed TA_2 achieves dual-band SLLs suppression by the amplitude/phase control, while maintaining a higher AE. Also, compared with the dual-band TAs with phase-only control in [9], [10], and [15], the designed TAs have the advantages of adjustable SLLs, smaller thickness and comparable bandwidth.

IV. CONCLUSION

In summary, we propose a novel dual-band transmissive MS with independent amplitude and phase control. To show its practical application, two TAs are simulated, fabricated and measured. The measured results are in good agreement with the simulated results. The proposed high-performance dual-band TAs have good application prospects in modern wireless communication systems and radar systems.

REFERENCES

[1] J. Y. Lau and S. V. Hum, "Reconfigurable transmitarray design approaches for beamforming applications," *IEEE Trans. Antennas Propag.*, vol. 60, no. 12, pp. 5679–5689, Dec. 2012.

[2] A. Clemente, L. Dussopt, R. Sauleau, P. Potier, and P. Pouliguen, "1-bit reconfigurable unit cell based on PIN diodes for transmit-array applications in X-band," *IEEE Trans. Antennas Propag.*, vol. 60, no. 5, pp. 2260–2269, May 2012.

[3] M. Feng et al., "Ultra-wideband and high-efficiency transparent coding metasurface," *Appl. Phys. A*, vol. 124, no. 9, pp. 1–8, Aug. 2018, Art. no. 630.

[4] F. F. Manzillo, A. Clemente, and J. L. González-Jiménez, "High-gain D-band transmitarrays in standard PCB technology for beyond-5G communications," *IEEE Trans. Antennas Propag.*, vol. 68, no. 1, pp. 587–592, Jan. 2020.

[5] X. Zhang, F. Yang, S. Xu, A. Aziz, and M. Li, "Dual-layer transmitarray antenna with high transmission efficiency," *IEEE Trans. Antennas Propag.*, vol. 68, no. 8, pp. 6003–6012, Aug. 2020.

[6] L. Yin et al., "Amplitude and phase independently adjustable transmitarray aperture and its applications to high gain and low sidelobe antenna," *IEEE Trans. Antennas Propag.*, vol. 70, no. 6, pp. 4498–4506, Jun. 2022.

[7] L.-X. Wu et al., "Transmissive metasurface with independent amplitude/phase control and its application to low-side-lobe metalens antenna," *IEEE Trans. Antennas Propag.*, vol. 70, no. 8, pp. 6526–6536, Aug. 2022.

[8] H. Li, G. Wang, T. Cai, H. Hou, and W. Guo, "Wideband transparent beamforming metadevice with amplitude- and phase-controlled metasurface," *Phys. Rev. Appl.*, vol. 11, no. 1, Jan. 2019, Art. no. 014043.

[9] R. Y. Wu, Y. B. Li, W. Wu, C. B. Shi, and T. J. Cui, "High-gain dual-band transmitarray," *IEEE Trans. Antennas Propag.*, vol. 65, no. 7, pp. 3481–3488, Jul. 2017.

[10] M. O. Bagheri, H. R. Hassani, and B. Rahmati, "Dual-band, dual-polarised metallic slot transmitarray antenna," *Microw., Antennas Propag.*, vol. 11, pp. 402–409, 2017.

[11] A. Aziz, F. Yang, S. Xu, M. Li, and H.-T. Chen, "A high-gain dual-band and dual-polarized transmitarray using novel loop elements," *IEEE Antennas Wireless Propag. Lett.*, vol. 18, no. 6, pp. 1213–1217, Jun. 2019.

[12] S. A. Matos et al., "High gain dual-band beam-steering transmit array for satcom terminals at Ka-band," *IEEE Trans. Antennas Propag.*, vol. 65, no. 7, pp. 3528–3539, Jul. 2017.

[13] T. Cai, G.-M. Wang, J.-G. Liang, Y.-Q. Zhuang, and T.-J. Li, "High-performance transmissive meta-surface for *C-/X*-band lens antenna application," *IEEE Trans. Antennas Propag.*, vol. 65, no. 7, pp. 3598–3606, Jul. 2017.

[14] A. Aziz, F. Yang, S. Xu, and M. Li, "An efficient dual-band orthogonally polarized transmitarray design using three-dipole elements," *IEEE Antennas Wireless Propag. Lett.*, vol. 17, no. 2, pp. 319–322, Feb. 2018.

[15] K. T. Pham, R. Sauleau, E. Fourn, F. Diaby, A. Clemente, and L. Dussopt, "Dual-band transmitarrays with dual-linear polarization at Ka-band," *IEEE Trans. Antennas Propag.*, vol. 65, no. 12, pp. 7009–7018, Dec. 2017.

[16] Q. Wang et al., "Broadband metasurface holograms: Toward complete phase and amplitude engineering," *Sci. Rep.*, vol. 6, no. 1, Sep. 2016, Art. no. 32867.

[17] Y. Ge, C. Lin, and Y. Liu, "Broadband folded transmitarray antenna based on an ultrathin transmission polarizer," *IEEE Trans. Antennas Propag.*, vol. 66, no. 11, pp. 5974–5981, Nov. 2018.

[18] D.-Y. Liu, M.-H. Li, X.-M. Zhai, L.-F. Yao, and J.-F. Dong, "Enhanced asymmetric transmission due to Fabry–Pérot-like cavity," *Opt. Exp.*, vol. 22, no. 10, pp. 11707–11712, 2014.

[19] Y. Wang et al., "Broadband high-efficiency ultrathin metasurfaces with simultaneous independent control of transmission and reflection amplitudes and phases," *IEEE Trans. Microw. Theory Techn.*, vol. 70, no. 1, pp. 254–263, Jan. 2022.

[20] W.-L. Guo, G.-M. Wang, X.-Y. Luo, K. Chen, H.-P. Li, and Y. Feng, "Dual-phase hybrid metasurface for independent amplitude and phase control of circularly polarized wave," *IEEE Trans. Antennas Propag.*, vol. 68, no. 11, pp. 7705–7710, Nov. 2020.

[21] L.-X. Wu, K. Chen, T. Jiang, J. Zhao, and Y. Feng, "Circular-polarization-selective metasurface and its applications to transmit-reflect-array antenna and bidirectional antenna," *IEEE Trans. Antennas Propag.*, vol. 70, no. 11, pp. 10207–10217, Nov. 2022.

[22] G. Ding, S. Chen, X.-Y. Luo, S.-Y. Wang, and K. Chen, "Ultrathin single-substrate Pancharatnam-Berry phase metasurface with high transmission efficiency," *IEEE Trans. Antennas Propag.*, vol. 71, no. 12, pp. 9571–9580, Dec. 2023.

[23] H.-P. Li, G.-M. Wang, T. Cai, J.-G. Liang, and X.-J. Gao, "Phase- and amplitude-control metasurfaces for antenna main-lobe and side-lobe manipulations," *IEEE Trans. Antennas Propag.*, vol. 66, no. 10, pp. 5121–5129, Oct. 2018.

[24] M. Wang, C. Huang, M. Pu, and X. Luo, "Reducing side lobe level of antenna using frequency selective surface superstrate," *Microw. Opt. Technol. Lett.*, vol. 57, no. 8, pp. 1971–1975, Aug. 2015.